

# Journal of Materials Chemistry A

Accepted Manuscript



This is an *Accepted Manuscript*, which has been through the Royal Society of Chemistry peer review process and has been accepted for publication.

*Accepted Manuscripts* are published online shortly after acceptance, before technical editing, formatting and proof reading. Using this free service, authors can make their results available to the community, in citable form, before we publish the edited article. We will replace this *Accepted Manuscript* with the edited and formatted *Advance Article* as soon as it is available.

You can find more information about *Accepted Manuscripts* in the [Information for Authors](#).

Please note that technical editing may introduce minor changes to the text and/or graphics, which may alter content. The journal's standard [Terms & Conditions](#) and the [Ethical guidelines](#) still apply. In no event shall the Royal Society of Chemistry be held responsible for any errors or omissions in this *Accepted Manuscript* or any consequences arising from the use of any information it contains.



## Enhanced thermoelectric properties of the Zintl phase BaGa<sub>2</sub>Sb<sub>2</sub> via doping with Na or K

Umut Aydemir,<sup>\*a,b</sup> Alex Zevalkink,<sup>c,d</sup> Alim Ormeci,<sup>d</sup> Sabah Bux,<sup>c</sup> and G. Jeffrey Snyder<sup>a,b</sup>

Received 00th January 20xx,  
Accepted 00th January 20xx

DOI: 10.1039/x0xx00000x

www.rsc.org/

Na- or K-doped samples of Ba<sub>1-x</sub>(Na, K)<sub>x</sub>Ga<sub>2</sub>Sb<sub>2</sub> were prepared by ball-milling followed by hot-pressing. The topological analysis of the electron density of BaGa<sub>2</sub>Sb<sub>2</sub> implies a polar covalent nature of the Sb–Ga bonds in which the Sb atoms receive the electrons transferred from Ba rather than the Ga atoms. Successful doping of BaGa<sub>2</sub>Sb<sub>2</sub> with Na or K was confirmed with combined microprobe and X-ray diffraction analysis. Alkali metal doping of BaGa<sub>2</sub>Sb<sub>2</sub> increased the *p*-type charge carrier concentration to almost the predicted optimum values ( $\sim 10^{20}$  h<sup>+</sup>/cm<sup>3</sup>) needed to achieve high thermoelectric performance. With increasing alkali metal concentration, electronic transport was shifted from non-degenerate semiconducting behaviour observed for BaGa<sub>2</sub>Sb<sub>2</sub> to degenerate one for Na- or K-doped compounds. Overall, the thermoelectric figure of merit, *zT*, values reached up to  $\sim 0.65$  at 750 K, considerably higher than the undoped sample (*zT*  $\sim 0.1$ ), and a slight improvement relative to previously reported Zn-doped samples ( $\sim 0.6$  at 800 K).

### 1. Introduction

Thermoelectric materials have many potential applications for the recovery of waste-heat energy.<sup>1, 2</sup> However, to be useful for broad applications, improved thermal to electrical energy conversion efficiencies are necessary. The thermoelectric efficiency of a material is determined by the dimensionless thermoelectric figure of merit, or  $zT = \alpha^2 T / \kappa \rho$ .<sup>3</sup> High *zT* materials must simultaneously exhibit high Seebeck coefficients (thermopower),  $\alpha$ , high electrical conductivity,  $\sigma = 1/\rho$  ( $\rho$  is electrical resistivity), and low thermal conductivity,  $\kappa$ . There are three contributions to thermal conductivity: the electronic contribution,  $\kappa_e$ , which is given by the Wiedemann-Franz law,  $\kappa_e = LT/\rho$ , where *L* is the Lorenz number, the bipolar contribution due to both electrons and holes,  $\kappa_b$ , and the lattice part,  $\kappa_L$ , which is due to phonons. The combination of desirable material properties is challenging to obtain, primarily because of the conflicting dependence of  $\alpha$ ,  $\rho$ ,  $\kappa_e$  and  $\kappa_b$  on the material's carrier concentration, *n*. In semiconductors, optimized carrier concentrations of  $n = 10^{19}$ - $10^{21}$  cm<sup>-3</sup> can typically be achieved by doping.

Zintl phases are a promising class of thermoelectric materials, characterized by complex anionic frameworks accommodating mainly ionically-bonded cations, such that the octet rule is satisfied.<sup>4, 5</sup> These compounds are often narrow

band gap semiconductors with exceptionally low lattice thermal conductivities due to their structural complexity.<sup>6</sup> Zintl compounds with diverse anionic structures have been shown to be promising thermoelectric materials. These range from isolated moieties (e.g., 14-1-11, Zn<sub>4</sub>Sb<sub>3</sub>),<sup>7-10</sup> to 1-dimensional chains or tetrahedra (e.g., 5-2-6, 3-1-3, 9-4-9),<sup>11-18</sup> 2-dimensional layers (e.g., 1-2-2, Mg<sub>3</sub>Sb<sub>2</sub>),<sup>19-21</sup> and 3-dimensional frameworks (e.g., clathrates, skutterudites, Mo<sub>3</sub>Sb<sub>7</sub>).<sup>22-29</sup>

So far, many 1-2-2 ternary pnictides have been revealed in the system *A*-(*T*, *Tr*)-*Pn* (*T* = Mg, Mn, Zn, Cd; *Tr* = Al, Ga, In; *Pn* = P, As, Sb) with divalent alkaline earth metals (e.g., *A* = Ca, Sr, Ba) and rare earths (e.g., *A* = Eu and Yb).<sup>30-38</sup> Most of the *A*-*T*-*Pn* phases crystallize in the well-known CaAl<sub>2</sub>Si<sub>2</sub> structure type including YbT<sub>2</sub>Sb<sub>2</sub>, EuZn<sub>2</sub>Pn<sub>2</sub>, EuMn<sub>2</sub>Pn<sub>2</sub>, CaMn<sub>2</sub>Pn<sub>2</sub> and SrMn<sub>2</sub>Pn<sub>2</sub>.<sup>30-32</sup> When the divalent transition metal is substituted with a triel element (e.g., Ga or In), completely different crystal structures are formed with two or three-dimensional polyanions (Fig. 1).<sup>33, 34</sup> For example, most phosphides and arsenides consist of polyanionic layers of  $[(Ga, In)_2(P, As)_2]^{2-}$  separated by divalent cations as in the case of BaGa<sub>2</sub>As<sub>2</sub> (Fig. 1d).<sup>35</sup> On the other hand both BaGa<sub>2</sub>Sb<sub>2</sub> and EuGa<sub>2</sub>Sb<sub>2</sub> are comprised of three dimensional polyanionic network of [Ga<sub>2</sub>Sb<sub>2</sub>]<sup>2-</sup> in which Ba and Eu atoms are aligned along the large tunnels in the *b*-axis (Fig 1 a, c).<sup>36-38</sup> Apparently, the size of the cationic filler determines the size of the cavities in which four rows of Ba atoms are fitted in one channel in BaGa<sub>2</sub>Sb<sub>2</sub> compared to two rows of Eu atoms in EuGa<sub>2</sub>Sb<sub>2</sub>. Moreover, the size of the pnictide atom is decisive for the dimensionality of the anionic structure (3D for Sb case and 2D for As and P cases).

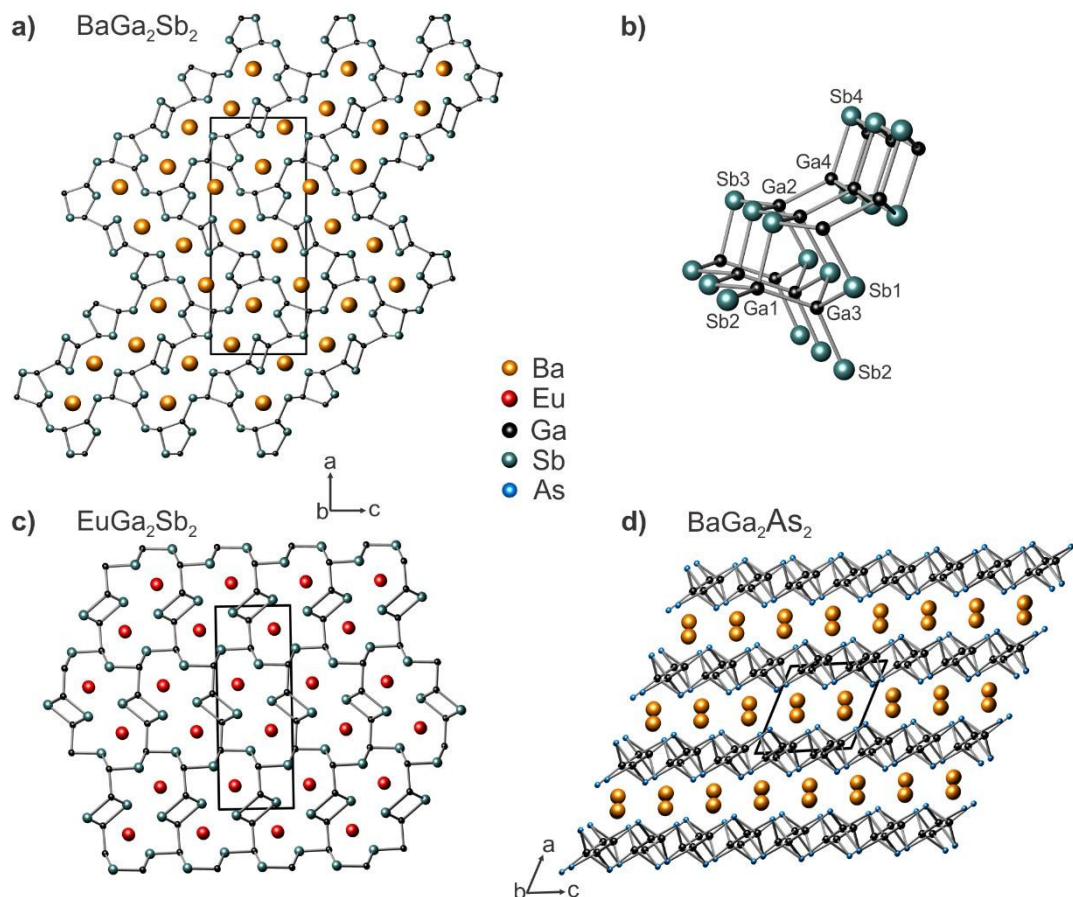
The Zintl phase BaGa<sub>2</sub>Sb<sub>2</sub> (space group *Pnma*, no. 62) was first reported by Kim *et al.*<sup>36</sup> Based on the simple Zintl counting, [Ba<sup>2+</sup>][(4b)Ga<sup>1-</sup>]<sub>2</sub>[(3b)Sb<sup>0</sup>]<sub>2</sub>, BaGa<sub>2</sub>Sb<sub>2</sub> is a charge

<sup>a</sup> Department of Applied Physics and Materials Science, California Institute of Technology, 1200 E California Blvd, Pasadena, CA 91125, USA

<sup>b</sup> Department of Materials Science and Engineering, Northwestern University, 2220 Campus Drive, Evanston, IL 60208, USA

<sup>c</sup> Thermal Energy Conversion Technologies Group, Jet Propulsion Laboratory, 4800 Oak Grove Drive, Pasadena, CA 91109, USA

<sup>d</sup> Max Planck Institute for Chemical Physics of Solids, Nöthnitzer Straße 40, Dresden 01187, Germany



balanced Zintl compound predicted to show semiconducting thermoelectric behavior. Recently, we reported on the high temperature **Fig. 1 a), c), d)** Crystal structures of three dimensional  $\text{BaGa}_2\text{Sb}_2$  and  $\text{EuGa}_2\text{Sb}_2$  and two dimensional  $\text{BaGa}_2\text{As}_2$  along the  $b$ -axis, respectively. **b)** Local arrangement of Ga and Sb atoms in the crystal structure of  $\text{BaGa}_2\text{Sb}_2$  with Ga-Ga dimers, distorted pentagons and ladder-like square chains.

properties of that compound and showed that substitution of Zn on the Ga site could be used to increase the carrier concentration and improve the thermoelectric properties.<sup>37</sup> Maximum  $zT$  values of  $\sim 0.6$  at 823 K were achieved in Zn-substituted samples. However, the carrier concentrations in these samples ( $\sim 5 - 8 \times 10^{19} \text{ h}^+/\text{cm}^3$  at room temperature) were slightly lower than the expected values, suggesting that alternative dopants might provide even better results. Motivated by previous studies in which alkaline earth metals were substituted by the alkali metals (*e.g.*,  $\text{Ca}_{5-x}\text{Na}_x\text{Al}_2\text{Sb}_6$ ,  $\text{Ca}_{3-x}\text{Na}_x\text{AlSb}_3$ ),<sup>39</sup> here we investigate the influence of Na or K substitutions on the Ba site in  $\text{BaGa}_2\text{Sb}_2$ . Additionally, density functional calculations and analysis of the electron localizability indicator are used to further characterize the bonding chemistry of  $\text{BaGa}_2\text{Sb}_2$ .

## 2. Experimental

### 2.1 Sample Preparation

GaSb was used as a precursor for the synthesis of undoped and doped  $\text{BaGa}_2\text{Sb}_2$ . For preparation of GaSb, stoichiometric amounts of Ga shot (Alfa Aesar, 99.99 %) and Sb shot Aesar, 99.999 %) were weighed and transferred to a quartz ampoule in

an Ar-filled glove box. The ampoule was then sealed under vacuum ( $\sim 10^{-6}$  mbar) and heat treated in a vertical furnace: heated up to 800 °C in 6 h, annealed there for 12 h and cooled down to room temperature in 6 h. For the synthesis of  $\text{BaGa}_2\text{Sb}_2$ , crystalline dendritic Ba (Alfa Aesar, 99.9 %) was cut into small pieces, mixed with GaSb and loaded into a steel vial together with two steel balls of  $\frac{1}{2}$  inch diameter. Ball-milling was carried out for 90 min. in Ar atmosphere by a SPEX Sample Prep 8000 Series Mixer/Mill. To obtain alkali metal doped samples, small pieces (1-2 mm) were cut from Na ingot (Alfa Aesar, 99.8 %) or K cubes (Alfa Aesar, 99.5 %) and mixed with stoichiometric amounts of Ba and GaSb for ball milling. For consolidation, samples were hand-ground in the glove box and placed in  $\frac{1}{2}$  inch diameter high-density graphite dies (POCO) and hot-pressed at 550 °C for 1 h under Ar atmosphere and 40 MPa pressure.

### 2.2 Sample Characterization

Sample purities were checked by X-ray diffraction (XRD) data using a Philips XPERT MPD diffractometer ( $\text{Cu-K}\alpha$  radiation) with reflection mode. The calculation of the lattice parameters using  $\alpha$ -Si as internal standard and the Rietveld refinements

were carried out with WinCSD program package.<sup>40</sup> Sample densities were measured with Archimedes' principle. Scanning electron microscopy (SEM) and energy dispersive X-ray spectroscopy (EDS) investigation was performed using a Zeiss 1550 VP Field Emission SEM equipped with Oxford X-Max SDD EDS system. The chemical compositions of the target phases were determined by microprobe analysis with wavelength dispersive X-ray spectroscopy (WDS, JEOL JXA - 8200 system) based on an average of 10 different measurement points on the bulk materials.

### 2.3 Transport Properties Measurements

Electrical and thermal transport properties were measured between 300 and 823 K. The electrical resistivity and Hall coefficient measurements were performed using Van der Pauw technique under a reversible magnetic field of 1 T (undoped sample) or 2 T (doped samples) using pressure-assisted tungsten electrodes.<sup>41</sup> The Seebeck coefficients of the samples were determined using chromel–Nb thermocouples by applying an oscillated temperature gradient of  $\pm 7.5$  K.<sup>42</sup> Thermal diffusivity,  $D$ , was measured with a Netzsch LFA 457 laser flash apparatus. Thermal conductivity was calculated using the relation:  $\kappa = D \times d \times C_p$ , in which  $d$  is the density of material being investigated (obtained by Archimedes' method) and  $C_p$  is the heat capacity at constant pressure. For  $C_p$ , the Dulong-Petit limit was used, which may lead to overestimation of the thermal conductivity values mainly at high temperatures.

### 2.4 Electronic Structure Calculations

The all-electron full-potential local orbital method (FPLO)<sup>43</sup> was used in the first-principles electronic structure calculations reported here. The local density approximation (LDA) as parametrized by Perdew-Wang<sup>44</sup> was employed. The crystal structure data for  $\text{BaGa}_2\text{Sb}_2$  were taken from Ref.<sup>36</sup>. A  $k$ -mesh of  $5 \times 28 \times 12$  giving 315 irreducible points was sufficient for converged results. Real space chemical bonding analysis was carried out by applying the concept of electron localizability indicator (ELI).<sup>45, 46</sup> Both electron density (ED) and ELI can be computed by first-principles electronic structure methods, and both of these computed quantities are scalar functions of the real space coordinates. Hence, the techniques of Bader's quantum theory of atoms in molecules (QTAIM)<sup>47</sup> are applicable to both. The ED-based analysis provides effective atomic charges. The ELI-based analysis enables us to determine how many electrons participate in each bond and how many atoms (centers) contribute to it. Individual atom contributions and the bond polarity can also be obtained by applying the basin intersection technique.<sup>48</sup> The ED and ELI calculated using a module implemented in the FPLO package<sup>49</sup> were analyzed by the program DGRID.<sup>50</sup> AVIZO software is used for ELI visualization.<sup>51</sup>

## 3. Results and Discussion

### 3.1 Phase Analysis

Nearly single phase  $\text{BaGa}_2\text{Sb}_2$  was obtained after ball-milling (Fig. 2). However, a partial decomposition to GaSb phase ( $\leq 2-3$  wt.%) was observed after hot-pressing, due probably to the sublimation of Ba during high temperature consolidation, as no Ba-containing secondary phase was detected by XRD or SEM analysis (Fig. 2, 3). The compositions of the target phases are tabulated in Table 1. According to the microprobe analysis, the determined chemical composition of  $\text{BaGa}_2\text{Sb}_2$  is almost the same as the nominal one. For Na- or K-substituted samples, although K content was found to increase with rising substitution level, the concentration of Na in the target phase remained almost constant suggesting that K has higher solubility in the crystal lattice than Na. The densities of disk-shaped samples were measured to be greater than 95 % of the theoretical value.

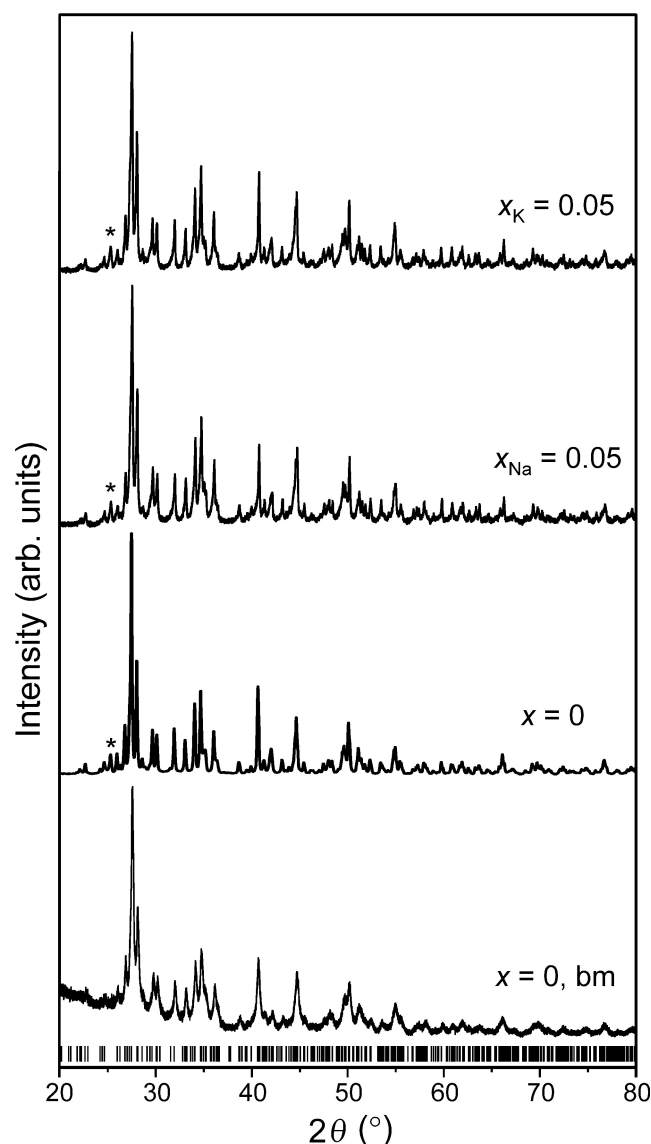


**Fig. 2** XRD patterns of ball-milled ( $x = 0$ , bm) and hot pressed ( $x = 0$ )  $\text{BaGa}_2\text{Sb}_2$  together with Na- or K-substituted samples ( $x_{\text{Na}} = 0.05$  and  $x_{\text{K}} = 0.05$ , respectively). Small amount of GaSb was precipitated in hot pressed samples, marked by asterisks. Ticks mark the theoretical peak positions of  $\text{BaGa}_2\text{Sb}_2$ .

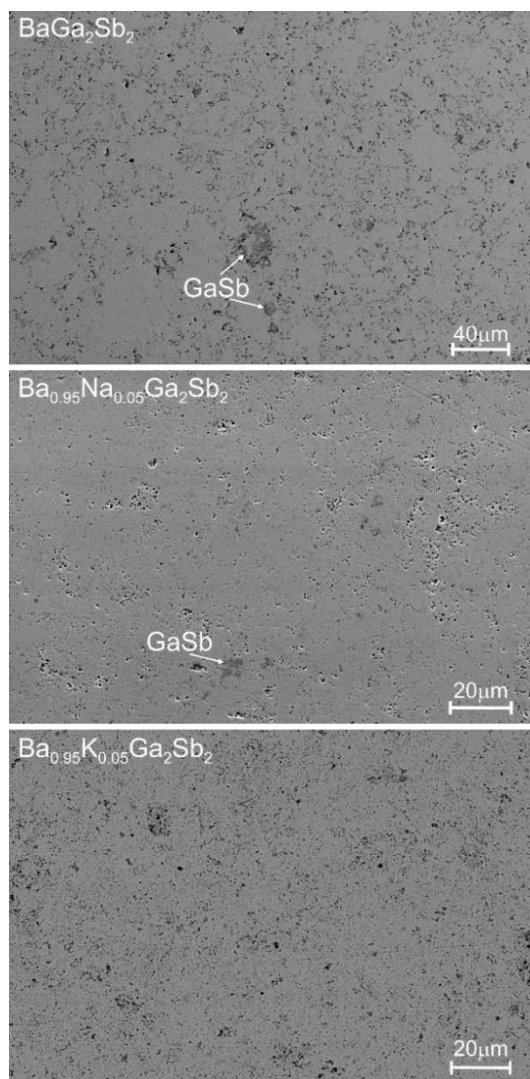


**Fig. 3** SEM images of  $\text{Ba}_{1-x}(\text{Na}, \text{K})_x\text{Ga}_2\text{Sb}_2$  ( $x = 0, 0.05$ ) samples in back-scattered electron mode. The secondary phase GaSb precipitated within the large grains of the target phases.

**Table 1:** The nominal and WDS compositions of the target phases together with standard uncertainties.

Nominal Comp.	WDS Comp.
$\text{BaGa}_2\text{Sb}_2$	$\text{Ba}_{1.014(3)}\text{Ga}_{1.99(1)}\text{Sb}_{1.999(8)}$
$\text{Ba}_{0.975}\text{Na}_{0.025}\text{Ga}_2\text{Sb}_2$	$\text{Ba}_{0.936(3)}\text{Na}_{0.037(4)}\text{Ga}_{2.06(1)}\text{Sb}_{1.970(9)}$
$\text{Ba}_{0.95}\text{Na}_{0.05}\text{Ga}_2\text{Sb}_2$	$\text{Ba}_{0.947(3)}\text{Na}_{0.035(4)}\text{Ga}_{2.05(1)}\text{Sb}_{1.964(9)}$
$\text{Ba}_{0.9}\text{Na}_{0.1}\text{Ga}_2\text{Sb}_2$	$\text{Ba}_{0.908(3)}\text{Na}_{0.041(4)}\text{Ga}_{2.07(1)}\text{Sb}_{1.981(9)}$

$\text{Ba}_{0.975}\text{K}_{0.025}\text{Ga}_2\text{Sb}_2$	$\text{Ba}_{0.953(3)}\text{K}_{0.010(1)}\text{Ga}_{2.07(1)}\text{Sb}_{1.964(9)}$
$\text{Ba}_{0.95}\text{K}_{0.05}\text{Ga}_2\text{Sb}_2$	$\text{Ba}_{0.935(3)}\text{K}_{0.028(1)}\text{Ga}_{2.07(1)}\text{Sb}_{1.970(9)}$
$\text{Ba}_{0.9}\text{K}_{0.1}\text{Ga}_2\text{Sb}_2$	$\text{Ba}_{0.894(3)}\text{K}_{0.067(1)}\text{Ga}_{2.06(1)}\text{Sb}_{1.982(9)}$

### 3.2 Crystal Structure

$\text{BaGa}_2\text{Sb}_2$  has a distinct crystal structure comprising large tunnels (open cages) running along the  $b$ -axis (Fig. 1a). These tunnels are formed by 26-membered rings of Ga and Sb atoms. In the framework, each Ga atom is four-fold coordinated with one Ga and three Sb atoms, while each Sb atom is three-fold coordinated with Ga atoms. Overall, six Sb atoms are connected to a Ga–Ga dimer forming  $[\text{Ga}_2\text{Sb}_{6/3}]^{2-}$  units with an ethane-like staggered conformation (Fig. 1b). Square nets (similar to  $\text{BaZn}_2\text{Sn}_2$ <sup>52</sup>) and five-membered rings of Ga and Sb atoms are formed in this way resulting in narrow tubes along the  $b$ -axis. In  $\text{BaGa}_2\text{Sb}_2$ , Ba atoms are accommodated in the open cages similarly found in intermetallic clathrates or clathrate-like structures.<sup>53–55</sup> The lattice parameters of undoped and doped samples are shown in Fig. 4. By substituting Ba with alkali metals, it was observed that  $b$  decreases, while  $a$  and  $c$  increase. The trend in volume is not monotonic: while it remains almost constant for Na-doped samples, the volume increases slightly for K-doped samples with  $x_K = 0.025$  and  $0.05$  and returns to almost the same value as the undoped compound for  $x_K = 0.1$  sample. As the doping efficiency was found to be lower than 100 % (see WDS results in Table 1), the presence of small amount of Na or K in the other atomic or interstitial sites should be considered, which is subject of our future project based on synchrotron X-ray and high resolution electron microscopy analysis.

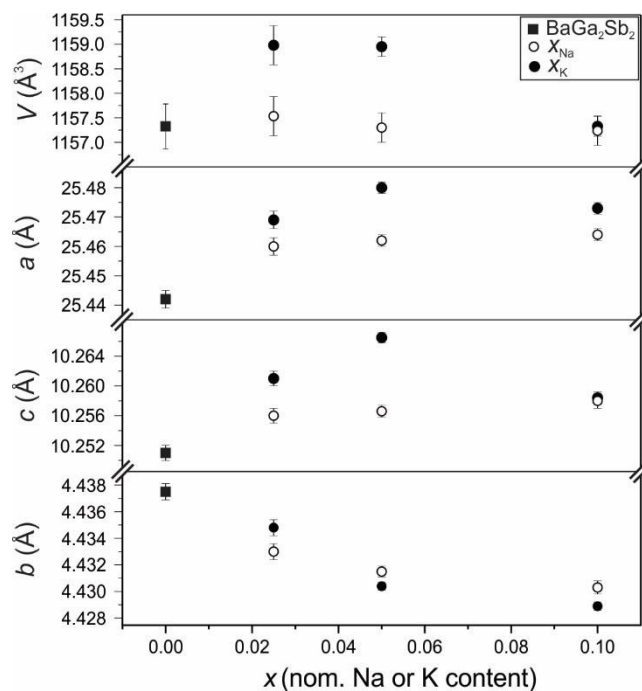


**Fig. 4** The lattice parameters and the volumes of  $\text{Ba}_{1-x}(\text{Na}, \text{K})_x\text{Ga}_2\text{Sb}_2$  samples with standard deviations.

The crystal structure of  $\text{BaGa}_2\text{Sb}_2$  possesses  $2 \times \text{Ba}$ ,  $4 \times \text{Ga}$  and  $4 \times \text{Sb}$  atomic positions (Wyck Symb  $4c : x, \frac{1}{4}, z$ ). The Rietveld refinements were performed for two representative compounds:  $\text{Ba}_{1.95}\text{Na}_{0.05}\text{Ga}_2\text{Sb}_2$  and  $\text{Ba}_{1.95}\text{K}_{0.05}\text{Ga}_2\text{Sb}_2$  (Fig. 5). All the Ga and Sb positions were considered to be fully occupied. The Ba sites were refined as mixed occupied with Na or K atoms. According to the Rietveld results, the compositions of these phases were determined to be  $\text{Ba}_{0.96}\text{Na}_{0.04}\text{Ga}_2\text{Sb}_2$  and  $\text{Ba}_{0.98}\text{K}_{0.02}\text{Ga}_2\text{Sb}_2$ , which are similar to the microprobe results.

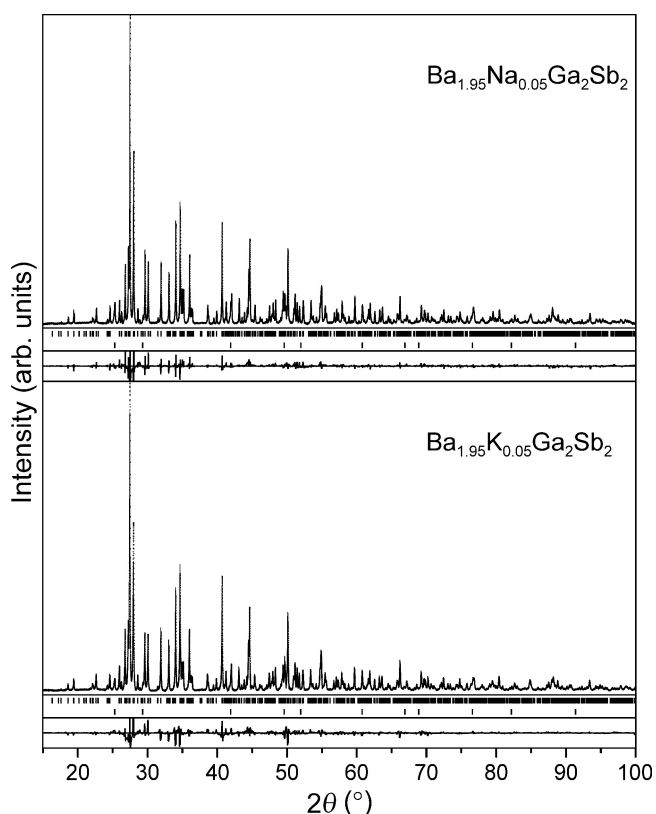


**Fig. 5** The Rietveld refinement plots for  $\text{Ba}_{1.95}\text{Na}_{0.05}\text{Ga}_2\text{Sb}_2$  and  $\text{Ba}_{1.95}\text{K}_{0.05}\text{Ga}_2\text{Sb}_2$  ( $\text{Cu-K}\alpha_1$  radiation). Upper and lower ticks mark the calculated reflection positions of the target phases and  $\text{GaSb}$ , respectively. The baselines correspond to the residuals of Rietveld refinements based on the reported structure model.<sup>36</sup>

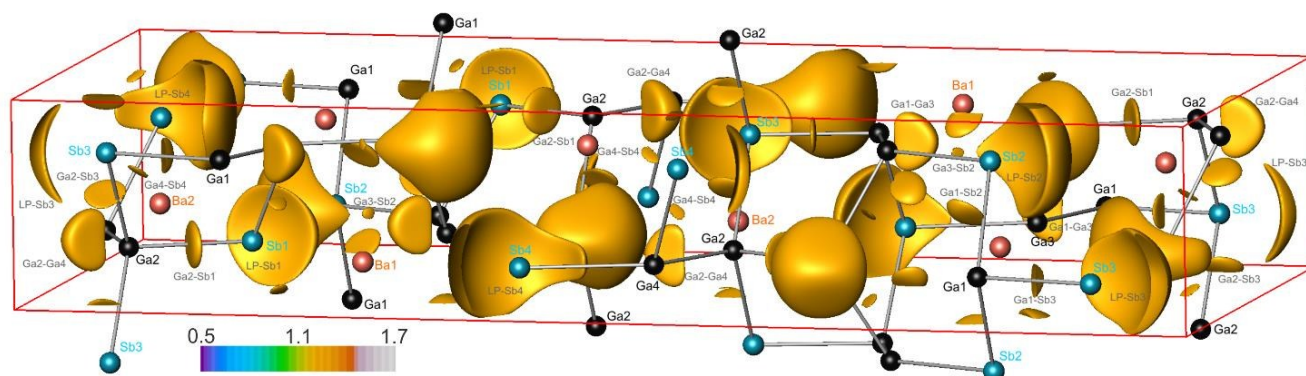


**Fig. 6** Bonding situation in  $\text{BaGa}_2\text{Sb}_2$  as depicted by the ELI isosurface plot with  $\gamma = 1.21$ . Ba, Ga and Sb atoms are shown in orange, black, and blue, respectively. Some of the two-center interactions and the lone-pair-like features of the Sb atoms are labeled.

### 3.3 Chemical Bonding in Real Space

The topological analysis of the electron density shows that the Ba atoms lose 1.2 electrons and the Sb atoms gain on average 0.6 electrons (actual values vary between 0.4 and 0.7) with the Ga atoms being approximately neutral (effective charges are in the range  $-0.05$  and  $0.05$ ). This finding implies that the Sb atoms rather than the expected Ga atoms are the recipients of the electrons transferred from the Ba atoms so that the implied charge balance looks like  $[\text{Ba}^{1.2+}][\text{Ga}^0][\text{Sb}^{0.6-}]_2$ . In order to understand this result we should examine the nature of the atomic interactions as revealed by the topological analysis of the ELI (Fig. 6).

As discussed in section 3.2, in  $\text{BaGa}_2\text{Sb}_2$  each Sb atom has three Ga neighbors, one in the same  $y$  layer and two equidistant in the adjacent  $y$  layers. Although Sb1, Sb2 and Sb3 have Ga neighbors from two different Wyckoff positions, Sb4 is coordinated only with Ga4. In addition to these Sb–Ga contacts there are two pairs of Ga–Ga contacts. Hence, each Ga atom has four near neighbors in total. According to the topological analysis of the ELI, there are three separate sets of attractors (local maxima of the ELI) for each Sb1, Sb2 and Sb3 atoms. One set represents the lone pair like interactions to which the Ba atoms contribute less than 5% of the corresponding basin's total electron population. These populations are 2.5, 2.9 and 2.8 for Sb1, Sb2 and Sb3, respectively. The other sets represent two-center Sb–Ga bonds. The number of electrons found in these bond basins range between 1.5 and 2.0. Sb contributions are between 1.2 and 1.7 times Ga contributions implying polar covalent interactions. This bond polarity is in agreement with the electronegativities of Ga and Sb, which are 1.81 and 2.05 in Pauling's scale,<sup>56</sup> respectively. In the case of Sb4, the attractors of the lone pair like feature and the ELI bond with the Ga4 atom in the same  $y$  layer merge into a single attractor. The resulting basin holds 4.5 electrons with Sb4 and Ga4 providing 3.8 and 0.6 electrons, respectively. Ba atom contributions are less than 2%. The remaining Sb4–Ga4 bonds have bond electron count and bond polarity values similar to those of the other Sb–Ga bonds. The Ga1–Ga3 bond contains 2.2 electrons with essentially equal contributions, whereas in the Ga2–Ga4 bond case, Ga4 contributes slightly more, 1.21 versus 1.06.

In summary, although the Ga atoms are four-coordinated and thereby expected to need four electrons according to the standard 2-center 2-electron scheme, we find that, the Sb–Ga bonds are of polar covalent nature, reflecting mainly the electronegativity difference between Ga and Sb, so that Ga contributions to these polar bonds are less than one electron. As a result, Ga atoms manage four bonds with three valence electrons, while the Sb

atoms end up receiving the electrons transferred from Ba.

### 3.4 Electronic Transport

BaGa<sub>2</sub>Sb<sub>2</sub> exhibits non-degenerate semiconducting behavior with a low  $p$ -type carrier concentration that increases exponentially with temperature (Fig. 7). Correspondingly, the resistivity is high and decreasing with temperature. As previously reported, the high temperature resistivity yields a band gap of 0.4 eV, which was also confirmed by optical absorption measurements.<sup>36, 37</sup> Due to its intrinsic behavior, the peak  $zT$  of BaGa<sub>2</sub>Sb<sub>2</sub> was limited to around 0.1, therefore, it was necessary to increase the carrier concentration to further increase  $zT$ . Previously, we showed that Zn substitutions (BaGa<sub>2-x</sub>Zn<sub>x</sub>Sb<sub>2</sub>) can be used to increase the carrier concentration and obtain extrinsic semiconducting behavior.<sup>37</sup> However, the maximum  $n$  achieved in this way was less than  $10^{20}$  h<sup>+</sup>/cm<sup>3</sup>, likely limited by low Zn solubility on the Ga site. Here, substitutions of either Na<sup>+</sup> or K<sup>+</sup> on the Ba<sup>2+</sup> site were employed as an alternative to Zn doping. As illustrated in Fig. 7a, Na and K are both effective as dopants in BaGa<sub>2</sub>Sb<sub>2</sub>, leading to decreased  $\rho$  and a transition to degenerate behavior.

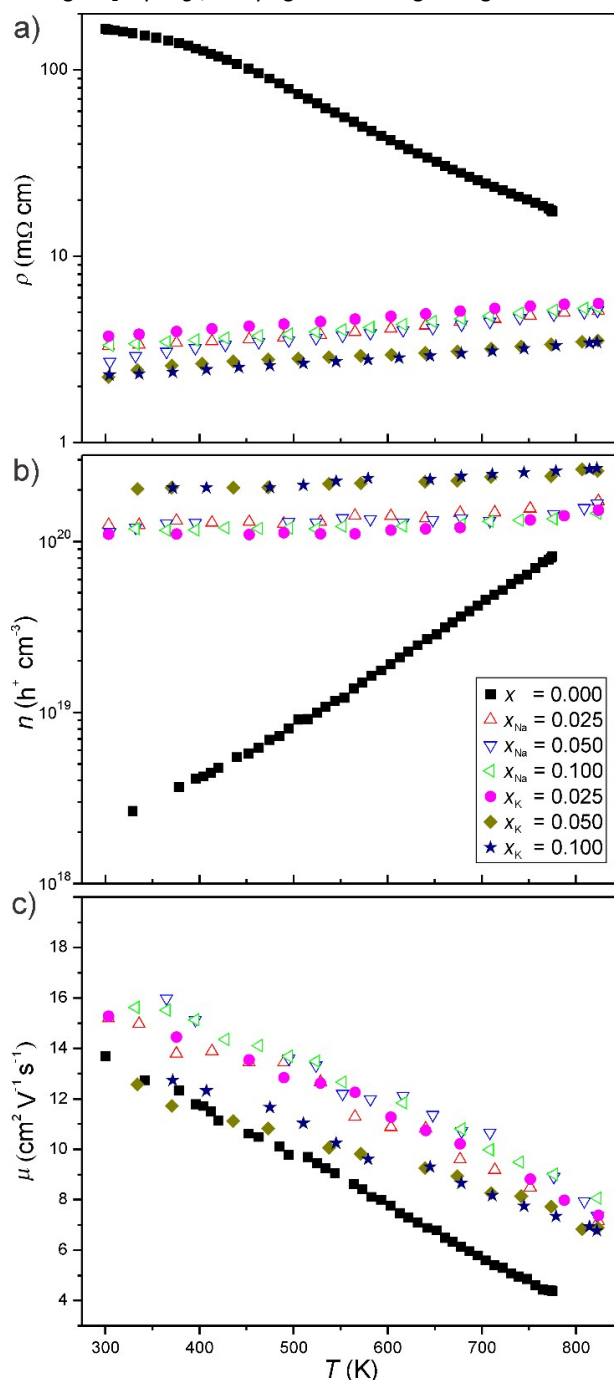
The predicted carrier concentration for Na or K substitutions of  $x = 0.025$  is  $n = 1.7 \times 10^{20}$  h<sup>+</sup> cm<sup>-3</sup>, assuming that each substitution of Na<sup>1+</sup> or K<sup>1+</sup> on a Ba<sup>2+</sup> site leads to one free hole (h<sup>+</sup>). Shown in Fig. 7b,  $x_{Na}=0.025$  and  $x_K=0.025$  samples have  $n_H \sim 1.2 \times 10^{20}$  h<sup>+</sup>/cm<sup>3</sup> experimentally. Thus, while less than 100 % efficient, Na and K are both more effective dopants than Zn in BaGa<sub>2-x</sub>Zn<sub>x</sub>Sb<sub>2</sub>. The carrier concentration plateaus beyond  $x = 0.025$  in Na-doped samples and beyond  $x = 0.050$  in K-doped samples, consistent with the lattice parameter behavior. The Hall mobility ( $\mu_H = 1/ne\rho$ ) is shown in Fig. 7c. For all the samples, the mobility decreases as temperature increases with  $\mu \propto T^{-p}$  ( $1.0 \leq p \leq 1.5$ ) indicative of transport limited by acoustic phonon scattering.<sup>57</sup> Surprisingly, the mobility of lightly doped K and Na samples are higher than that of BaGa<sub>2</sub>Sb<sub>2</sub>. It is likely that  $n_H$  of the undoped sample has been overestimated due to the assumption of a single carrier type in the relation  $R_H = 1 / (n_H \times e)$  (where  $R_H$  is the Hall coefficient). This can then lead to an underestimation of the mobility in intrinsic semiconductors.

The Seebeck coefficients,  $\alpha$ , of samples are shown in Fig. 8a and b as a function of temperature and carrier concentration, respectively. With increasing Na or K content, the Seebeck coefficients decrease and show an increasingly linear temperature dependence. The curves in Fig. 8b were calculated using a single parabolic band model (SPB) assuming a constant effective band mass of  $1.7 m_e$  and acoustic phonon scattering.<sup>57</sup> The same effective mass can be used to fit K-, Na-, or Zn-doped samples. The calculated and measured Seebeck values were found to be very similar, indicating that the electronic transport can be explained adequately by the SPB model.

### 3.5 Thermal Transport

The total thermal conductivity of Na- or K-substituted samples is shown in Fig. 9a. The electronic contribution,  $\kappa_e$ , was estimated using the Wiedemann-Franz relation as described above with Lorenz numbers ( $L$ ) calculated using an SPB model (inset of Fig. 9b). Subtracting  $\kappa_e$  from the total thermal conductivity yields the lattice ( $\kappa_l$ ) and bipolar contributions ( $\kappa_b$ ), shown in Fig. 9b. In general, the

lattice thermal conductivity is the dominant contribution for all samples over the entire temperature range. The bipolar term becomes less significant with increased carrier concentration. The measured  $\kappa_l$  of all samples remains higher than the calculated  $\kappa_{min}$ ,<sup>37</sup> which suggests that further efforts should be directed to lowering  $\kappa_l$  by *e.g.*, alloying or lowering the grain size of the



samples to create more scattering centers for heat carrying phonons.

**Fig. 7 a)** The resistivity of Na- or K- substituted samples increases linearly with temperature, and **b)** the carrier concentrations are relatively temperature-independent, typical of degenerate semiconductors. **c)** Na or K substitutions lead to increased mobility in BaGa<sub>2</sub>Sb<sub>2</sub>.

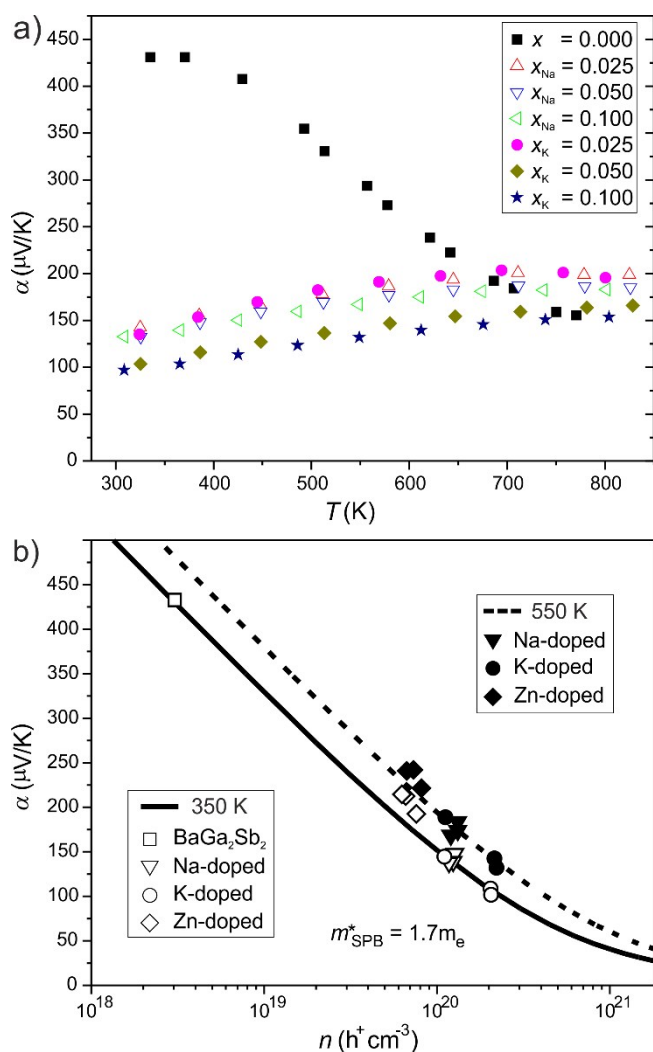


**Fig. 8 a)** The Seebeck coefficients decrease with increasing K and Na content, showing the linear temperature dependence expected for degenerate semiconductors when  $x > 0.50$ . **b)** The  $n$ -dependence of the Seebeck coefficients can be described using an SPB model with  $m^* = 1.7m_e$  at 350 and 550 K.

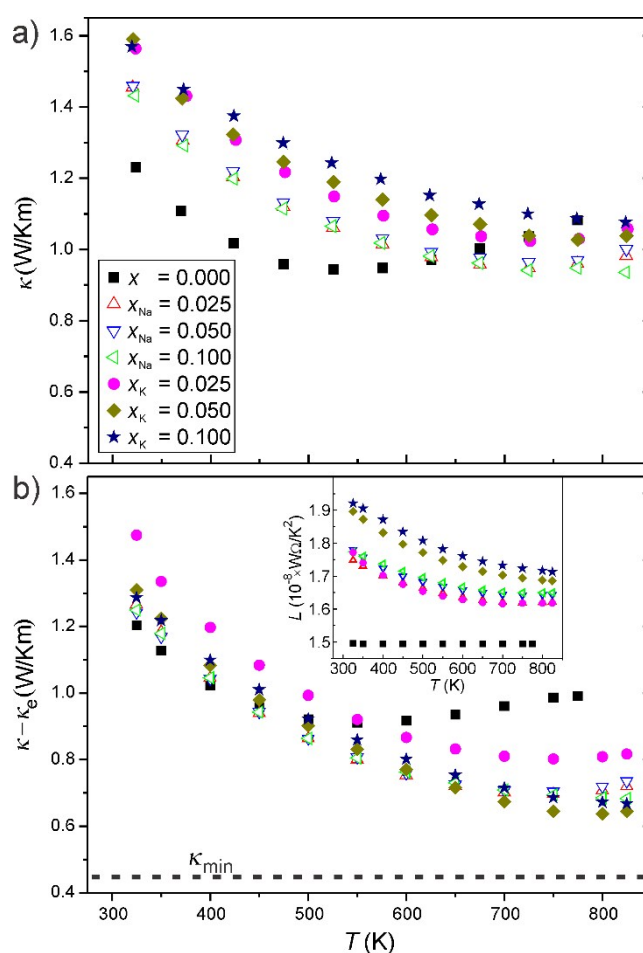


**Fig. 9 a)** Total and **b)** lattice plus bipolar thermal conductivity of  $\text{Ba}_{1-x}(\text{Na}, \text{K})_x\text{Ga}_2\text{Sb}_2$  samples.

### 3. 6 Thermoelectric Figure of Merit

The figure of merit, or  $zT$ , for each sample was calculated by polynomial fitting of the experimental data (Fig. 10a). Due to low carrier concentration and intrinsic behavior, undoped  $\text{BaGa}_2\text{Sb}_2$  sample shows a peak  $zT$  of around 0.1 at 600 K. The values are increased dramatically by alkali metal doping, reaching up to 0.65 at 750 K, which is a slightly higher than previously reported Zn-doped samples ( $\sim 0.6$  at 800 K).<sup>37</sup> To check if the optimum concentration levels are achieved, the  $n$ -dependence of Lorenz number, mobility and Seebeck coefficients was calculated based on the SPB model, which was used to estimate  $zT$  as a function of  $n$ , by assuming a constant  $\kappa_L$  (Fig. 10b). The following parameters were used in the model:  $\mu_0 = 17 \text{ cm}^2/\text{Vs}$ ,  $\kappa_L = 0.81 \text{ W/Km}$ , and  $m_{\text{SPB}}^* = 1.7 m_e$ . Details of the equations and assumption used in this model can be found in Ref. [57]. Based on Fig. 10b, the optimum carrier concentration ( $1\text{--}2 \times 10^{20} \text{ h}^+/\text{cm}^3$ ) was reached and even surpassed (for the case of  $x_{\text{K}} = 0.05, 0.1$ ) by alkali metal substitution in  $\text{BaGa}_2\text{Sb}_2$ . It was shown in the previous study that at very high carrier concentrations, single parabolic band behavior can no longer be expected for  $\text{BaGa}_2\text{Sb}_2$ , as additional bands are expected to contribute to transport.<sup>37</sup> However, evidence of such behavior was not observed within the carrier concentration range achieved in this study.

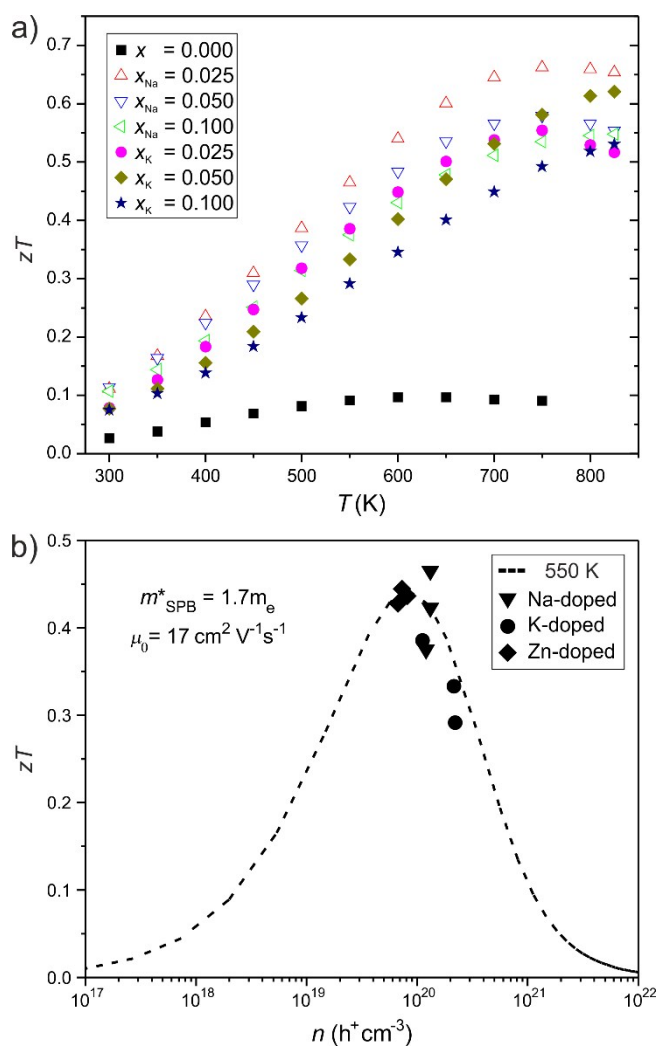


**Fig. 10** a) The temperature dependence of  $zT$  of the  $\text{Ba}_{1-x}(\text{Na, K})_x\text{Ga}_2\text{Sb}_2$  samples. b) Experimental  $zT$  values at 550 K show that the carrier concentration is nearly optimized within an SPB model at this temperature.

#### 4. Conclusions

Na- and K-doped samples of  $\text{Ba}_{1-x}(\text{Na, K})_x\text{Ga}_2\text{Sb}_2$  ( $x = 0, 0.025, 0.05, 0.1$ ) were successfully prepared. According to the topological analysis of the ELI, the Sb–Ga bonds in  $\text{BaGa}_2\text{Sb}_2$  are of polar covalent nature and Sb atoms receive the electrons rather than Ga atoms transferred from Ba. Successful substitution of K or Na on the Ba site up to  $x \sim 0.07$  was confirmed by lattice constant refinements and microprobe analysis. The  $p$ -type carrier concentrations increased with increasing K or Na content, leading to a transition from nondegenerate to degenerate semiconducting behaviour of the resistivity and Seebeck coefficients. The doping effectiveness of alkali metals on the Ba site in  $\text{BaGa}_2\text{Sb}_2$  was found to be higher with K than with Na, but in both cases higher than achieved previously using Zn on the Ga site. The optimum carrier concentrations were achieved with values reaching  $\sim 10^{20} \text{ h}^+\text{cm}^{-3}$ , resulting in considerably high peak  $zT$  value of  $\sim 0.65$  at 750 K.

#### Acknowledgment

U. A. acknowledges the financial assistance of The Scientific and Technological Research Council of Turkey. This research was carried out in part at the Jet Propulsion Laboratory, California Institute of Technology, under a contract with the National Aeronautics and Space Administration and was supported by the NASA Science Missions Directorate's Radioisotope Power Systems Technology Advancement Program. We would like to acknowledge the Molecular Materials Research Center (MMRC) at Caltech for allowing use of their instruments for the optical measurements obtained in this work. A. O. thanks Ulrike Nitzsche from IFW Dresden, Germany for technical help in computational work.

#### Notes and references

1. T. M. Tritt, *Annu Rev Mater Res*, 2011, **41**, 433-448.
2. G. J. Snyder and E. S. Toberer, *Nat Mater*, 2008, **7**, 105-114.
3. D. M. Rowe, *Thermoelectrics Handbook : Macro to Nano*, CRC ; London : Taylor & Francis [distributor], Boca Raton, Fla., 2006.
4. S. M. Kauzlarich, *Chemistry, Structure, and Bonding of Zintl Phases and Ions*, VCH, New York ; Cambridge, 1996.
5. T. F. Fässler, *Zintl Phases: Principles and Recent Developments*, Springer, 2011.
6. S. M. Kauzlarich, S. R. Brown and G. J. Snyder, *Dalton Trans.*, 2007, DOI: Doi 10.1039/B702266b, 2099-2107.
7. S. R. Brown, S. M. Kauzlarich, F. Gascoin and G. J. Snyder, *Chem Mater*, 2006, **18**, 1873-1877.
8. E. S. Toberer, C. A. Cox, S. R. Brown, T. Ikeda, A. F. May, S. M. Kauzlarich and G. J. Snyder, *Adv Funct Mater*, 2008, **18**, 2795-2800.
9. G. J. Snyder, M. Christensen, E. Nishibori, T. Caillat and B. B. Iversen, *Nat Mater*, 2004, **3**, 458-463.
10. J. P. Lin, X. D. Li, G. J. Qiao, Z. Wang, J. Carrete, Y. Ren, L. Z. Ma, Y. J. Fei, B. F. Yang, L. Lei and J. Li, *J Am Chem Soc*, 2014, **136**, 1497-1504.
11. A. Zevalkink, J. Swallow and G. J. Snyder, *Dalton Trans.*, 2013, **42**, 9713-9719.
12. U. Aydemir, A. Zevalkink, A. Ormeci, H. Wang, S. Ohno, S. Bux and G. J. Snyder, *Dalton Trans.*, 2015, **44**, 6767-6774.
13. A. Zevalkink, J. Swallow, S. Ohno, U. Aydemir, S. Bux and G. J. Snyder, *Dalton Trans.*, 2014, **43**, 15872-15878.
14. A. Zevalkink, W. G. Zeier, G. Pomrehn, E. Schechtel, W. Tremel and G. J. Snyder, *Energy Environ. Sci*, 2012, **5**, 9121-9128.
15. A. Zevalkink, E. S. Toberer, W. G. Zeier, E. Flage-Larsen and G. J. Snyder, *Energy Environ. Sci*, 2011, **4**, 510-518.
16. S. K. Bux, A. Zevalkink, O. Janka, D. Uhl, S. Kauzlarich, J. G. Snyder and J. P. Fleurial, *J Mater Chem A*, 2014, **2**, 215-220.
17. S. Ohno, A. Zevalkink, Y. Takagiwa, S. K. Bux and G. J. Snyder, *J Mater Chem A*, 2014, **2**, 7478-7483.
18. S. Chanakian, U. Aydemir, A. Zevalkink, Z. M. Gibbs, J.-P. Fleurial, S. Bux and G. Jeffrey Snyder, *J Mater Chem C*, 2015, **3**, 10518-10524.
19. G. S. Pomrehn, A. Zevalkink, W. G. Zeier, A. van de Walle and G. J. Snyder, *Angew. Chem.*, 2014, **126**, 3490-3494.
20. A. Bhardwaj, A. Rajput, A. K. Shukla, J. J. Pulikkotil, A. K. Srivastava, A. Dhar, G. Gupta, S. Auluck, D. K. Misra and R. C. Budhani, *RSC Adv*, 2013, **3**, 8504-8516.
21. A. Bhardwaj and D. K. Misra, *RSC Adv*, 2014, **4**, 34552-34560.
22. Y. Saiga, B. Du, S. K. Deng, K. Kajisa and T. Takabatake, *J Alloy Compd*, 2012, **537**, 303-307.
23. H. Zhang, H. Borrmann, N. Oeschler, C. Candolfi, W. Schnelle, M. Schmidt, U. Burkhardt, M. Baitinger, J. T. Zhao and Y. Grin, *Inorg Chem*, 2011, **50**, 1250-1257.

24. X. Shi, J. Yang, S. Bai, J. Yang, H. Wang, M. Chi, J. R. Salvador, W. Zhang, L. Chen and W. Wong-Ng, *Adv Funct Mater*, 2010, **20**, 755-763.
25. C. Uher, *Semiconduct Semimet*, 2001, **69**, 139-253.
26. T. He, J. Z. Chen, H. D. Rosenfeld and M. A. Subramanian, *Chem Mater*, 2006, **18**, 759-762.
27. Y. Tang, Y. Qiu, L. Xi, X. Shi, W. Zhang, L. Chen, S.-M. Tseng, S.-w. Chen and G. J. Snyder, *Energy Environ. Sci*, 2014, **7**, 812-819.
28. X. Shi, Y. Pei, G. J. Snyder and L. Chen, *Energy Environ. Sci*, 2011, **4**, 4086-4095.
29. C. Candolfi, B. Lenoir, A. Dauscher, B. Malaman, E. Guilmeau, J. Hejtmanek and J. Tobola, *Appl Phys Lett*, 2010, **96**, 262103.
30. I. Schellenberg, M. Eul, W. Hermes and R. Pöttgen, *Z. Anorg. Allg. Chem.*, 2010, **636**, 85-93.
31. G. Cordier and H. Schäfer, *Z. Naturforsch. B Chem. Sci.*, 1976, **31**, 1459.
32. S. Bobev, J. Merz, A. Lima, V. Fritsch, J. D. Thompson, J. L. Sarrao, M. Gillessen and R. Dronskowski, *Inorg Chem*, 2006, **45**, 4047-4054.
33. J. Jiang and S. M. Kauzlarich, *Chem Mater*, 2006, **18**, 435-441.
34. A. M. Goforth, H. Hope, C. L. Condrón, S. M. Kauzlarich, N. Jensen, P. Klavins, S. MaQuilon and Z. Fisk, *Chem Mater*, 2009, **21**, 4480-4489.
35. H. He, R. Stearrett, E. R. Nowak and S. Bobev, *Inorg Chem*, 2010, **49**, 7935-7940.
36. S. J. Kim and M. G. Kanatzidis, *Inorg Chem*, 2001, **40**, 3781-3785.
37. U. Aydemir, A. Zevalkink, A. Ormeci, Z. M. Gibbs, S. Bux and G. J. Snyder, *Chem Mater*, 2015, **27**, 1622-1630.
38. I. Schellenberg, M. Eul and R. Pottgen, *Monatsh Chem*, 2011, **142**, 875-880.
39. A. Zevalkink, G. J. Snyder and S. M. Haile, Thesis (Ph D ), California Institute of Technology, 2014.
40. L. Akselrud and Y. Grin, *J Appl Crystallogr*, 2014, **47**, 803-805.
41. K. A. Borup, E. S. Toberer, L. D. Zoltan, G. Nakatsukasa, M. Errico, J. P. Fleurial, B. B. Iversen and G. J. Snyder, *Rev Sci Instrum*, 2012, **83**, 123902.
42. S. Iwanaga, E. S. Toberer, A. LaLonde and G. J. Snyder, *Rev Sci Instrum*, 2011, **82**, 063905.
43. H. E. K. Koepernik, *Phys. Rev. B*, 1999, **59**, 1743-1757.
44. J. P. Perdew and Y. Wang, *Phys. Rev. B*, 1992, **45**, 13244-13249.
45. M. Kohout, *Faraday Discuss*, 2007, **135**, 43-54.
46. F. R. Wagner, V. Bezugly, M. Kohout and Y. Grin, *Chem-Eur J*, 2007, **13**, 5724-5741.
47. R. F. W. Bader, *Atoms in Molecules : A Quantum Theory*, Clarendon Press, Oxford, 1990.
48. S. Raub and G. Jansen, *Theor Chem Acc*, 2001, **106**, 223-232.
49. A. Ormeci, H. Rosner, F. R. Wagner, M. Kohout and Y. Grin, *J Phys Chem A*, 2006, **110**, 1100-1105.
50. M. Kohout, program DGRID, Radebeul, Germany, 2011
51. Visualization Sciences Group, software AVIZO, www.avizo3d.com, Oregon, USA
52. U. Aydemir, A. Zevalkink, S. Bux and G. J. Snyder, *J Alloy Compd*, 2015, **622**, 402-407.
53. U. Aydemir, L. Akselrud, W. Carrillo-Cabrera, C. Candolfi, N. Oeschler, M. Baitinger, F. Steglich and Y. Grin, *J Am Chem Soc*, 2010, **132**, 10984-10985.
54. C. Candolfi, U. Aydemir, A. Ormeci, W. Carrillo-Cabrera, U. Burkhardt, M. Baitinger, N. Oeschler, F. Steglich and Y. Grin, *J Appl Phys*, 2011, **110**, 043715
55. S. Bobev and S. C. Sevov, *Inorg Chem*, 2000, **39**, 5930-5937.
56. J. Emsley, *The elements*, Clarendon Press ; Oxford University Press, Oxford, New York, 3rd edn., 1998.
57. A. F. May and G. J. Snyder, in *Materials, Preparation and Characterization in Thermoelectrics*, ed. D. M. Rowe, Taylor & Francis Group, Boca Raton, FL, 2012, pp. 11-11, 11-18.

## Enhanced thermoelectric properties of the Zintl phase $\text{BaGa}_2\text{Sb}_2$ via doping with Na or K

Umut Aydemir,<sup>\*a,b</sup> Alex Zevalkink,<sup>c,d</sup> Alim Ormeci,<sup>d</sup> Sabah Bux,<sup>c</sup> and G. Jeffrey Snyder<sup>a,b</sup>

### Graphical Text:

Carrier tuning of  $\text{BaGa}_2\text{Sb}_2$  by Na or K doping significantly enhance the thermoelectric efficiency ( $zT \sim 0.65$  at 750 K).

### Graphic:

